Journal of Fluids and Structures 17 (2003) 1001–1016

JOURNAL OF FLUIDS AND STRUCTURES

www.elsevier.nl/locate/jnlabr/yjfls

Aeroelastically deflecting flaps for shock/boundary-layer interaction control

D. Gefroh[a], E. Loth[a,*], C. Dutton[b], E. Hafenrichter[b]

[a] *Department of Aeronautical and Astronautical Engineering, University of Illinois at Urbana-Champaign, Urbana, IL 61801, USA*
[b] *Department of Mechanical and Industrial Engineering, University of Illinois at Urbana-Champaign, Urbana, IL 61801, USA*

Received 27 August 2001; accepted 1 April 2003

Abstract

An aeroelastic mesoflap system has been developed to improve the downstream flow properties of an oblique shock/boundary-layer interaction. The mesoflap system employs a set of small flaps over a cavity, whereby the flaps downstream of the interaction bend downward aeroelastically to bleed the flow and the upstream flaps bend upward to re-inject this same mass flow upstream. This recirculating system requires no net mass bleed and therefore has advantages for boundary layer control in external or mixed-compression supersonic aircraft inlets. In addition, the system may be applicable in other aerospace applications where boundary-layer control can help remedy the adverse effects of shock interactions. Several mesoflap systems have been fabricated and examined experimentally to investigate their aerodynamic and structural performance. Each mesoflap is rigidly attached to a spar on its upstream end while the remainder of the flap is free to deflect aeroelastically. The flap length is nominally a few boundary-layer thicknesses in dimension, while the flap thickness is small enough to allow tip deflections that are of the order of the boundary-layer momentum thickness. Experiments were conducted for a Mach 2.41 impinging oblique shock wave interaction with a turbulent boundary layer. Spanwise-centered laser Doppler velocimeter measurements indicate that certain mesoflap designs can show significant flow improvement as compared to the solid-wall case, including increased stagnation pressure recovery and a 7% reduction in boundary layer thickness and sonic thickness. However, one drawback of the mesoflap system is the potential for fatigue, which in some cases led to microcracking followed by flap failure. Structural design improvements to alleviate and avoid this problem included a lower profile spar design, substitution of Nitinol for aluminum as the flap material, and use of stress-relieving holes at the ends of the flap cut-outs.

1. Introduction

1.1. Bleed for shock/boundary-layer interaction (SBLI) control

When a supersonic boundary layer is subjected to the strong adverse pressure gradient caused by an impinging shock wave, the outgoing boundary layer is severely distorted and can become separated if the shock is sufficiently strong. A conventional method to counter the deleterious effects of this interaction is to apply mass bleed near the interaction. This has been used, in particular, in aerospace applications of supersonic inlets. Fig. 1 shows a schematic of a supersonic mixed-compression inlet where boundary layer bleed is used to reduce separation at the shock impingement locations. The bleed bands are used for both the internal oblique shock as well as the terminating normal shock

*Corresponding author. Tel.: +1-217-244-5581; fax: +1-217-244-0720. 306 Talbot Laboratory, 104 South Wright Street, Urbana, IL 61801-2935, USA.
E-mail address: e-loth@uiuc.edu (E. Loth).

0889-9746/03/$ - see front matter
doi:10.1016/S0889-9746(03)00053-7

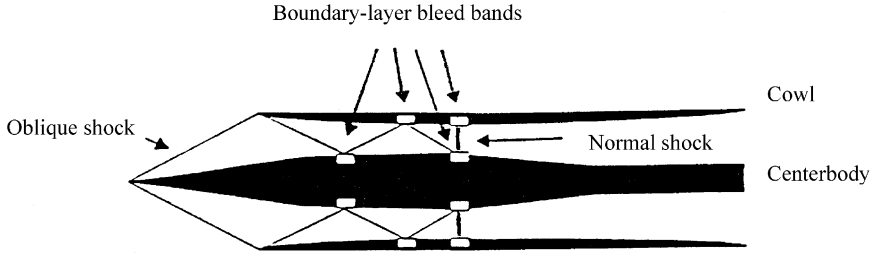

Fig. 1. A mixed-compression supersonic inlet with boundary-layer bleed (Laurendeau, 1995).

interactions with the engine cowl and centerbody boundary layers. Most engine inlets on military aircraft operating at speeds above Mach 2 employ active bleed control, which requires ducting of bleed flow to an external surface where it is discharged (Gridley and Walker, 1996). The bleed flow is typically removed through aligned or staggered holes or slots that cover a low-pressure plenum. Harloff and Smith (1996) summarize various bleed methodologies currently used by supersonic inlet designers. They indicate that the bleed holes in oblique shock regions are ideally inclined as much as 20° relative to the local surface to minimize bleed-induced drag. In the terminating normal shock region, the holes are typically set at 90° to aid in shock stability. Empirical scaling laws indictate that the ratio of hole diameter to boundary displacement thickness (D/δ^*) should be of the order of unity. In practice, actual engine inlets err on the side of conservatism by bleeding over a significant portion of the inlet with bleed rates approximately 25% higher than theoretical values (Syberg and Hickcox, 1973). The amount of bleed required increases significantly with flight Mach number and is on the order of 10–15% of the engine mass flow rate for Mach 3. Associated penalties, including drag, weight, and cost of the overall vehicle, are directly related to this bleed flow percentage.

1.2. Recirculation for SBLI control

Recirculating (or "passive") flow control of the SBLI region has been suggested as a promising method to reduce the detrimental effects of strong shock waves, especially for supersonic engine inlets (Stanewsky et al., 1997). This method of control involves establishing natural circulation within an enclosed cavity that spans the oblique or normal shock interaction region. The pressure difference across the shock is communicated through a porous medium to the cavity, thereby causing transpiration to occur without active suction. The result is injection upstream of the interaction to effectively reduce the shock strength and suction downstream to bleed off the boundary layer, thereby reducing separation. Since there is no net mass removal, bleed ducting and dumping systems are eliminated, along with their associated weight, volume, and cost penalties (Loth, 2000). Such recirculation transpiration for boundary layer control has the potential to reduce or eliminate flow separation in SBLIs, diffuse the shock footprint, and also stabilize the shock position.

The porous media experimentally and numerically tested to date have primarily consisted of holes and slots, both slanted and normal (Raghunathan, 1988; Raghunathan and McIlwain, 1990; Hamed et al., 1995). Success with recirculating transpiration has been limited due to insufficient rates of transpiration caused by limits on surface porosity and hole geometry (Bur et al., 1998), and increased drag penalties for no-shock or off-design flow conditions due to plate roughness (Laurendeau, 1995). While tangential injection and suction are desired for optimal SBLI transpiration effects, current systems employing this method require a priori knowledge of shock position and, therefore, may perform poorly at off-design conditions. There have been no attempts to use the concept of aeroelastic flaps in combination with the recirculating transpiration concept; this is the goal of the present study.

The current concept consists of a matrix of mesoflaps (of the scale of a few boundary layer thicknesses in length) covering an enclosed cavity as shown in Fig. 2. Each of the flaps is rigidly fixed over a small portion of its upstream end, but can deflect aeroelastically at its downstream end based on the pressure difference between the supersonic flow above and the subsonic cavity flow below. Under no-shock conditions, i.e., subsonic flow, the pressures above and below the flaps are nearly equal such that no deflections occur and no transpiration is induced. Since the surface is nearly aerodynamically smooth for the case of no-shock impingement, the roughening of the surface caused by conventional transpiration holes or slots is reduced.

Since the cavity pressure tends to be between the low pressure of the preshocked flow and the high pressure of the shocked flow, the flaps upstream of the impingement location will deflect upwards, allowing flow injection angled into

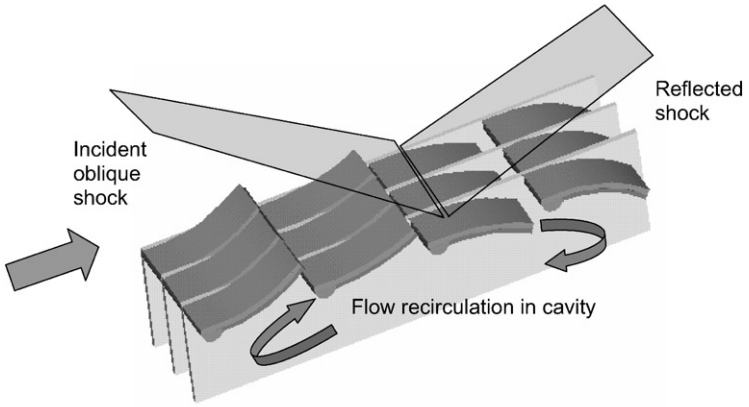

Fig. 2. Conceptual drawing of a two-dimensional MART array undergoing aeroelastic deflection (flow is from left to right).

the boundary layer. Additionally, the downstream flaps will deflect downward to allow angled bleed from the boundary layer into the cavity. As such, the gas dynamic pressure loads cause the flaps to deflect in a cantilever mode that coincides with the desired angled bleed and injection; i.e., the flaps are aeroelastically "smart." The resulting system is termed MART (Mesoflaps for Aeroelastic Recirculating Transpiration). The system was first studied numerically by Wood et al. (1999) and is considered experimentally herein.

In summary, the MART concept features four distinct advantages for SBLI control: (i) It retains the simplicity of a conventional passive-transpiration system (eliminating bleed airflow ducting and dumping). (ii) The geometry allows desirable bleed and injection aerodynamics (i.e., increased sonic mass coefficient) by employing angled transpiration. (iii) It allows variable streamwise position and sweep angle of the shock while retaining angled transpiration (to allow for variations of flight/inlet conditions). (iv) The MART system allows aerodynamic efficiency in subsonic flow (i.e., skin friction consistent with that of a solid wall), as the system will revert to a nearly smooth flat plate in this condition.

The objective of the present study is to experimentally assess the applicability of the MART system to control turbulent boundary layers with an impinging oblique shock wave. In particular, the structural performance of the flaps (ability to withstand the SBLI loads) and the aeroelastic transpiration performance (to improve the outgoing boundary-layer characteristics) were investigated. For comparison to the mesoflap cases, a solid-wall case was used as a baseline to quantify any aerodynamic performance improvements, while a microporous plate was used to demonstrate the difference between MART and a conventional fixed-geometry recirculating transpiration concept.

2. Experimental methods

2.1. Flow facility

The experiments reported here were conducted in a planar, two-dimensional, supersonic wind tunnel (a detailed description and schematic is given in Gefroh, 2000). The facility nozzle was designed for a nominal exit plane Mach number of 2.45 with an exit height of 50.8 mm and throat height of 18.4 mm. The test-section width (50.8 mm) is constant from the exit of the nozzle to the exit of the tunnel, yielding a square cross-section over a length of over 200 cm. The flow remains supersonic throughout this length and is then exhausted through a subsonic diffuser The measured Mach number just before the shock interaction was 2.41 (due to boundary layer growth) yielding a test-section freestream unit Reynolds number of $57 \times 10^6\,\mathrm{m}^{-1}$, based on a stagnation temperature of 300 K and a stagnation pressure of 581 kPa. An 8° shock generator is installed on the upper wall of the test-section (beginning at 8.2 cm downstream of the nozzle contour) to produce an oblique shock that impinges on the lower wall of the wind tunnel. The combined static pressure rise across the incident and reflected shock is 50.0 kPa. A cavity covered by an array of mesoflaps was centered at the oblique shock impingement location on the lower wall of the test-section. The cavity is 44.5 mm long, 19.1 mm deep, and spans the entire width of the tunnel test-section (50.8 mm). The lower wall with the cavity is removable and can be replaced with a solid wall to perform no-bleed baseline studies. At the shock-generator

start location, the boundary layer on the lower wall is fully turbulent with a 99.5% thickness (δ_0) of 4.0 mm and a momentum thickness of 0.30 mm, with $Re_\theta = 17\,200$.

2.2. Mesoflap configurations

Four generations of aluminum mesoflaps (shown in Fig. 3) and a nickel microporous plate were used to evaluate the effectiveness of using recirculating flow to control SBLIs. The microporous skin, termed GAC 1897, is a Northrop Grumman nickel plate with hourglass-shaped holes. Hwang (2000) investigated this porous surface extensively in no-shock supersonic flow in an effort to reduce turbulent skin friction with microblowing. These NASA-Glenn tests found that the microblowing technique with the GAC 1897 plate reduced skin friction by almost 75% at the largest blowing rate. The skin thickness is 305 μm, and the holes have an hourglass shape with larger diameters at the top and bottom surfaces, but narrowing to a smaller throat diameter of 60 μm in the middle of the plate. The porosity based on the openings at the skin surface is 50%, but is only 4% open based on the hole throat diameter.

The flap arrays were created by making cuts (each flap is defined by a spanwise cut connected by two streamwise cuts upstream at the spanwise edges) on a single sheet of metal and then bonding this sheet to a stringer plate which contained spars underneath the upstream portion of the flap. This technique was chosen to avoid mechanical fasteners which may adversely roughen the boundary layer and cause shock waves and to allow all the flaps in an array to be made from an integral piece. The first-generation aluminum mesoflaps were machined from a sheet of 127 μm thick 4003 H-18 aluminum shim stock. The cut width (the spanwise and streamwise gaps along the end and sides of the flap as viewed from above) on the sheet was 0.8 mm. The four flaps spanned $\frac{3}{4}$ of the tunnel width, and each was 9.2 mm long, yielding a flap width-to-streamwise length aspect ratio of 4.14 (see Fig. 3a). Supporting spars between individual flaps (and below the surface skin) were built into the aluminum frame and had a near-hemispherical shape on the underside (with a radius of approximately 1.3 mm). The surface skin portion of the aluminum that covered the spars (i.e., the spacing between successive flaps) had a streamwise length of 1.5 mm.

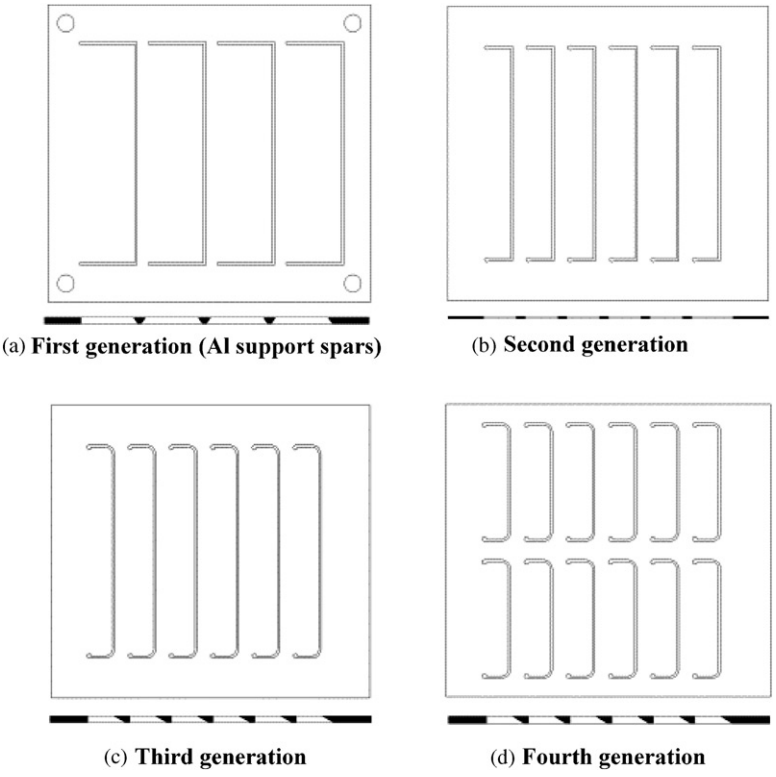

Fig. 3. Schematics of mesoflap designs (flaps shown with top view; below each flap set is a side view of the stringer support where the spars can be seen). The SBLI flow (on top the flaps) is from left to right.

Table 1
Mesoflap characteristics

	Generation 1	Generation 2	Generation 3	Generation 4
Material	4003 H-18 Al	4003 H-18 Al	7075-T6 Al, Nitinol	7075-T6 Al
Thickness (μm)	127	76.2–254	50.8–127	76.2–127
Number of flaps	4	6	6	12
Flap length (mm)	9.20	4.63	4.63	4.63
Flap aspect ratio	4.14	8.25	8.25	4.46
Streamwise flap spacing (mm)	1.50	2.38	2.38	2.38
Stringer support	Aluminum, 1.30 mm thick	Steel, 0.340 mm thick	Steel, 1.19 mm thick	Steel, 1.19 mm thick
Design evolution	Initial concept	Steel stringer	Thicker stringer *w/* angled spars	Matrix design with two rows of flaps
		Reduced flap length	Superior grade of aluminum	
		Reduced flap cut thickness	First use of Nitinol	
			Stress-relieving holes and rounded flap corners	

The second-generation design incorporated many improvements over its predecessor. In an effort to prevent deflections beyond the sonic line of the incoming boundary layer, the new flaps were reduced in length by about a factor of two and the number of flaps was increased from four to six. The cut width was also reduced to approximately 0.4 mm to reduce the amount of airflow that can recirculate in the undeflected state and to help increase the streamwise orientation of the injected airflow when deflection did occur. To reduce the stress concentration and the potential for microcrack formation, stress-relieving holes (0.8 mm diameter) were drilled at the furthest upstream end of the streamwise side cuts, which defined the outer edges of each flap. The new flaps were 4.63 mm long (as measured from the edge of the stress-relieving hole to the beginning of the spanwise cut) and also spanned $\frac{3}{4}$ of the wind tunnel width for a new aspect ratio of 8.25. The streamwise spacing between successive flaps was increased to 2.38 mm to provide increased area for bonding the aluminum sheet onto the spar support. In addition, the spar beneath each flap was no longer integral to the frame. Instead, a 0.44 mm thick steel stringer array was sandwiched between the flap array and the frame (see Fig. 3b). The stringer array is simply a 57.15 mm long $\times$ 50.8 mm wide steel plate with a series of rectangular cuts to allow for flap deflection. The resulting spanwise rectangular spars were 1.59 mm wide, resulting in a 0.79 mm overhang of the flap array material to allow for angled transpiration.

Design of the third-generation flaps was driven by problems regarding structural integrity that arose from the tests of the second-generation arrays (see Section 3). The third-generation flaps possess the same length, width, and spacing attributes as its second-generation predecessor (see Fig. 3c). The material, however, was changed to aerospace-grade 7075 T-6 aluminum, which possesses higher yield and fatigue strengths than the first- and second-generation material, with an equal modulus of elasticity. Additionally, the flap corners (connections between the spanwise cut and the streamwise cuts as seen from above) were rounded to a radius of 1.59 mm to prevent the formation of microcracks at the previously sharp corners. The stress-relieving holes were offset towards the array center-line such that they are tangent to the outer edge of the streamwise cut. The stringer thickness was increased three-fold, from 397 to 1190 μm, and the spanwise-running spar width was extended to eliminate the previous flap array overhang. To prevent flow blockage into the cavity, the leading edge of each spar was machined to a triangular shape (30° to the streamwise direction).

The fourth-generation aluminum flap array possesses is simply a two-dimensional matrix version of the third-generation design (see Fig. 3d). The matrix consists of two spanwise columns of six flaps that have the same streamwise length as the third-generation flaps. The flaps are 20.64 mm wide for an aspect ratio of 4.46. The columns have a spacing of 3.175 mm on either side. Underneath, the stringer support is identical to the third-generation stringer, except that it has a streamwise-running support spar down the middle.

The evolution of the mesoflap characteristics for the four generations is summarized in Table 1.

2.3. Investigation techniques

The efficacy of the MART system in controlling SBLI flows was evaluated using shadowgraph flow visualizations, surface pressure distributions, and laser Doppler velocimetry (LDV) measurements in the evolving boundary layer. Fused-silica windows in the tunnel sidewalls offer a viewable area of 18.5 cm (streamwise) × 3.9 cm (transverse), centered on the SBLI region. Single-frame shadowgraph photography was used to qualitatively visualize the oblique shock waves, expansion fans, and boundary-layer turbulence structure. For the solid-wall case, static pressure taps were placed along the spanwise center-line of the lower wall of the tunnel with a streamwise spacing of 3.18 mm. This allowed determination of the streamwise static pressure distribution from $-18\delta_0$ to $+17\delta_0$, as measured from the shock impingement location on the lower wall. For the mesoflap cases, no surface static pressure taps were included between $-7\delta_0$ to $+7\delta_0$, but instead static pressure taps were placed along the bottom wall of the cavity.

LDV is a nonintrusive technique that provides a direct measurement of the local velocity that is independent of the fluid properties, and can be used for SBLIs (Carroll and Dutton, 1992; Palko and Dutton, 1999). The present study utilized a one-component LDV setup (streamwise velocity component) to allow high spatial resolution near the wall in the event that the SBLI causes a region of flow reversal. A 5 W Spectra-Physics argon-ion laser was used in conjunction with a TSI fiber-optic system to transmit, receive, and process the scattered light signals. A Bragg cell opto-acoustical method was used to resolve flow direction ambiguity in the separated region near the wall. The probe volume diameter was 119.0 μm and the length (spanwise direction) was 5.54 mm. Forward scatter with an offset angle of 15° was used to maximize the data rate, increase the signal-to-noise ratio, and reduce the effective probe volume length to 0.97 mm.

Artificial seeding was employed in the LDV investigation using a TSI six-jet silicone oil atomizer. The polydispersed silicone oil droplets have a mean diameter of approximately 0.8 μm and have been found in previous studies to follow the turbulent fluctuations of flows of this type (Bloomberg, 1989; Amatucci, 1990). The LDV measurements were obtained along the spanwise mid-plane of the test-section, along wall-normal traverses at various axial locations. For the present investigation, the ensemble of instantaneous velocity realizations at each spatial location consisted of 4096 measurements. The overall maximum uncertainties in the calculation of the mean velocity and turbulence intensity are 2.0% and 0.79% of the free-stream approach velocity ($U_0 = 569$ m/s), respectively. The instantaneous realizations were velocity de-biased based on particle interarrival time (Herrin and Dutton, 1993). A detailed description of the uncertainty estimates is given in Gefroh (2000).

3. Results and discussion

3.1. Mesoflap aeroelastic behavior

As described in the previous section, four generations of mesoflap designs have been developed and tested, each one improving upon the previous iteration in terms of aerodynamic performance and structural integrity. Since flap deflection is theoretically proportional to streamwise length cubed and inversely proportional to thickness cubed, the flap geometry is crucial to the performance of the MART system.

In general terms, the mesoflap arrays deflected under aeroelastic loads as anticipated, i.e., the flaps upstream of impingement deflected up and those downstream deflected down to allow for angled bleed. It was found that the flaps that deflected the greatest amount were the leading and trailing flaps, while the middle flaps remained approximately undeflected during the experiments. In some cases, the wind tunnel testing caused individual flaps to fail structurally, i.e., they deformed plastically, developed microcracks at critical locations, or were completely severed from the array. Failure always occurred first for the upstream flaps, as the aeroelastic loads acted to tear them away from the stringer to which they were epoxied. Once the epoxy bond was compromised, microcracks formed and quickly propagated. Thus, the primary mode of failure is believed to be due to fatigue failure from oscillating loads during steady state operation (imperceptible to the naked eye) and/or during startup and especially shutdown (detectable with the unaided eye).

The first-generation MART arrays (see Fig. 3a) were 127 μm thick and each possessed four streamwise-spaced mesoflaps. Early tests of the first-generation mesoflaps were characterized by epoxy failure and rapid structural failure of the flaps themselves after only one tunnel run. Deflections were on the order of 20°, enough to cause failure from quasi-static loading during steady state, supersonic operation. Based on these results, it was decided to add the stress-relieving holes and to increase the ratio of flap thickness-to-streamwise length.

Several second-generation flap arrays (see Fig. 3b) were manufactured and tested, with thicknesses ranging from 76.2 to 254 μm, using improved epoxy for bonding to the steel stringer. It was found that the thicker flaps (152 to 254 μm) withstood the stresses induced by the supersonic flow, but did not deflect predominantly in a cantilever-type mode. Instead, undesired spanwise deflection of the support spars was detected. For the thinner cases (76.2 to 127 μm), larger

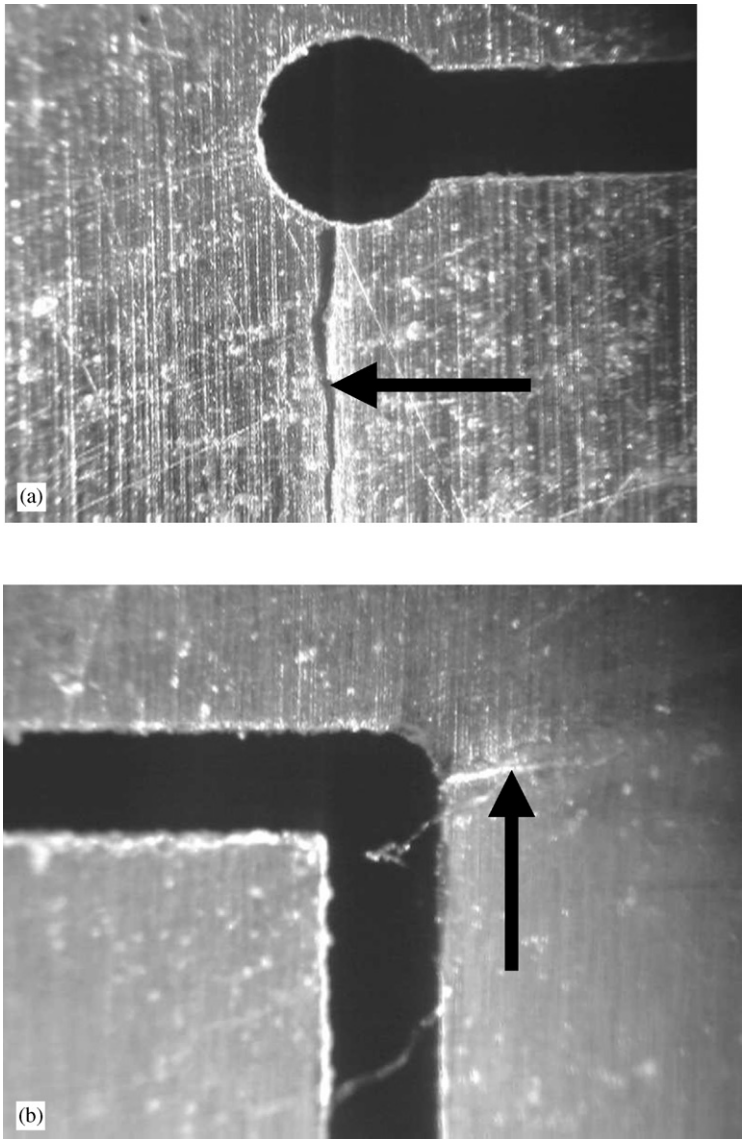

Fig. 4. Microphotographs showing cracks on aluminum surface skin of second-generation mesoflaps, where: (a) arrow indicates a spanwise crack initiating at stress-relief hole and running inwards and (b) arrow indicates a streamwise crack initiating at the downstream corner cut. For length scale reference, the cut width is about 400 μm in both cases.

cantilever deflections (on the order of 15° for the 76.2 μm flaps) were observed with only slight spanwise deflection. These thinner flaps yielded promising results (Gefroh et al., 2000a), but tended to fail after only a few tunnel runs (only one run for the 76.2 μm case). Interestingly, it was observed that the flaps would flutter briefly during tunnel startup and shutdown, but not at steady state. Failure occurred most frequently during shutdown when brief exposure to subsonic and/or transonic velocities apparently excited a natural frequency of the flap system and yielded many large-amplitude deflections. In such cases, microcracks (e.g., Fig. 4a) were initiated at the corners of the flaps, and propagated (both streamwise and spanwise) until the flap was torn from the array. Also, fracture was sometimes noted at the sharp corners (Fig. 4b). Typically, once the integrity of one flap was compromised, other flaps soon followed, and the entire array was then lost.

The third-generation design (Fig. 3c) focused on thinner arrays (76.2 to 127 μm) due to the minimal deflection of the second-generation mesoflaps of thicknesses larger than 127 μm. By increasing the stringer thickness (from 397 to

1190 μm), these mesoflaps deflected exclusively in the cantilever mode, thus eliminating the spanwise bending found in the second-generation mesoflaps. As a result, the third-generation cantilever deflections were larger than those of its predecessor for equal flap thicknesses, e.g., 20° deflections for the 76.2 μm mesoflap array (about 25% greater than that for the second-generation 76.2 μm design). In general, the offset of the stress-relief holes (to allow the flap array to be fully supported by the stringer) reduced the occurrence of spanwise microcracks (as shown in Fig. 4a for the second-generation mesoflaps), while rounding the trailing edges of the flaps reduced the streamwise microcrack problems (noted in Fig. 4b). However, with the increased deflections and thinner flaps of the third-generation geometry, structural integrity was still an issue. In particular, the 76.2 μm mesoflap array failed during shutdown-induced oscillations (albeit after a few runs instead of only one). In addition to the fatigue failure, the deflections of these thinnest arrays caused the flaps to deform plastically, indicating that a material which allows larger elastic strains would be helpful to explore the full potential of the MART concept.

In order to increase the structural reliability of the MART system, aluminum was replaced by Nitinol (nickel–titanium alloy) as the sheet material for additional third-generation experiments. Nitinol possesses roughly the same stiffness as aluminum (E of approximately 70 GPa), but allows two to three times larger flap deflections before deforming plastically. Use of Nitinol for the mesoflaps dramatically improved resistance to microcracks and flap fatigue. In particular, the 76.2 μm Nitinol array did not exhibit failure as noted in the aluminum case, and an even thinner 50.8 μm Nitinol array was able to withstand several wind tunnel runs (Gefroh et al., 2000b). Due to the additional resilience of this material, an electric discharge machine was used to accurately fabricate the mesoflap arrays from the Nitinol sheets. As expected, the overall aerodynamic performance for the 76.2 μm Nitinol array was similar to that for the 76.2 μm aluminum array (Gefroh et al., 2000a, b), which indicates that the only difference was mechanical (i.e., resistance to structural failure) and not aerodynamic.

The fourth-generation arrays (Fig. 3d) were simply two-dimensional versions of the third-generation arrays. These were fabricated to study the effect of flap aspect ratio on overall aerodynamic and structural performance. Deflections were consistent with those found for the third-generation design, but the spanwise variation in flap deflection was reduced. For conciseness, this paper discusses the flow measurement results for only the aluminum mesoflap cases in the following sections, since the aerodynamic performance was equivalent with the Nitinol mesoflaps of the same thickness and overall geometry.

3.2. Shadowgraph flow visualizations

The typical features of a classic SBLI are identifiable in the shadowgraph of Fig. 5a, which shows the flow over the solid wall at the location of shock impingement (flow direction from left to right). The incident shock clearly impinges on the lower wall, then reflects and coalesces close to the wall, with a shock front developed as a result of the rapid thickening of the boundary layer near the impingement point. A slip line indicating the presence of a shear layer internal to the boundary layer was also observed to initiate at the intersection of the incident and reflected shocks. This slip line persisted beyond 50 mm downstream of the interaction where it was approximately 3.5 mm above the tunnel floor. This location correlates well with measurements of high turbulence intensity in the boundary layer. The expansion fan emanating from the downstream tip of the shock-generator wedge can be seen entering the top of the picture and impinging on the boundary layer edge approximately 44 mm downstream of shock impingement. This corresponds to $x^* = 11$, where $x^* = (x - x_0)/\delta_0$, with x_0 corresponding to the middle of the cavity (also the approximate shock impingement location), and δ_0 corresponding to the incoming boundary-layer thickness (4 mm).

Shadowgraph images were also obtained for several different thicknesses of mesoflap arrays. A typical image of SBLI control using the MART concept is shown in Fig. 5b with a 127 μm thick second-generation flap array. The leading oblique shock previously associated with the rapid thickening of the wall boundary layer in the solid-wall case was located further upstream at a position over the first flap. This compression-corner-type shock is clear evidence of the upward deflection of the upstream flaps, coupled with injection of cavity flow from this flap location, and is typical of other work on recirculation control of SBLIs (e.g., Squire, 1998). Diffusion of the shock interaction and expansion waves was also observed downstream of the shock impingement location; this and other features can also be noted in numerical simulations of the flow field reported by Wood et al. (1999). There is also a trailing compression wave that originates at the downstream end of the cavity for the thinner flaps, and is caused by the angled supersonic bleed flow over the last flap.

Fourth-generation MART shadowgraphs were obtained to evaluate the three-dimensional effects associated with having two rows of mesoflaps instead of only one. Fig. 5c shows a shadowgraph of a 127 μm thick, fourth-generation array. Although these three-dimensional effects are integrated along the spanwise direction with the shadowgraph technique, subtle differences can be identified when compared against the second-generation array in Fig. 5b. In particular, the downstream boundary layer thickness appears slightly greater for the fourth-generation design. This

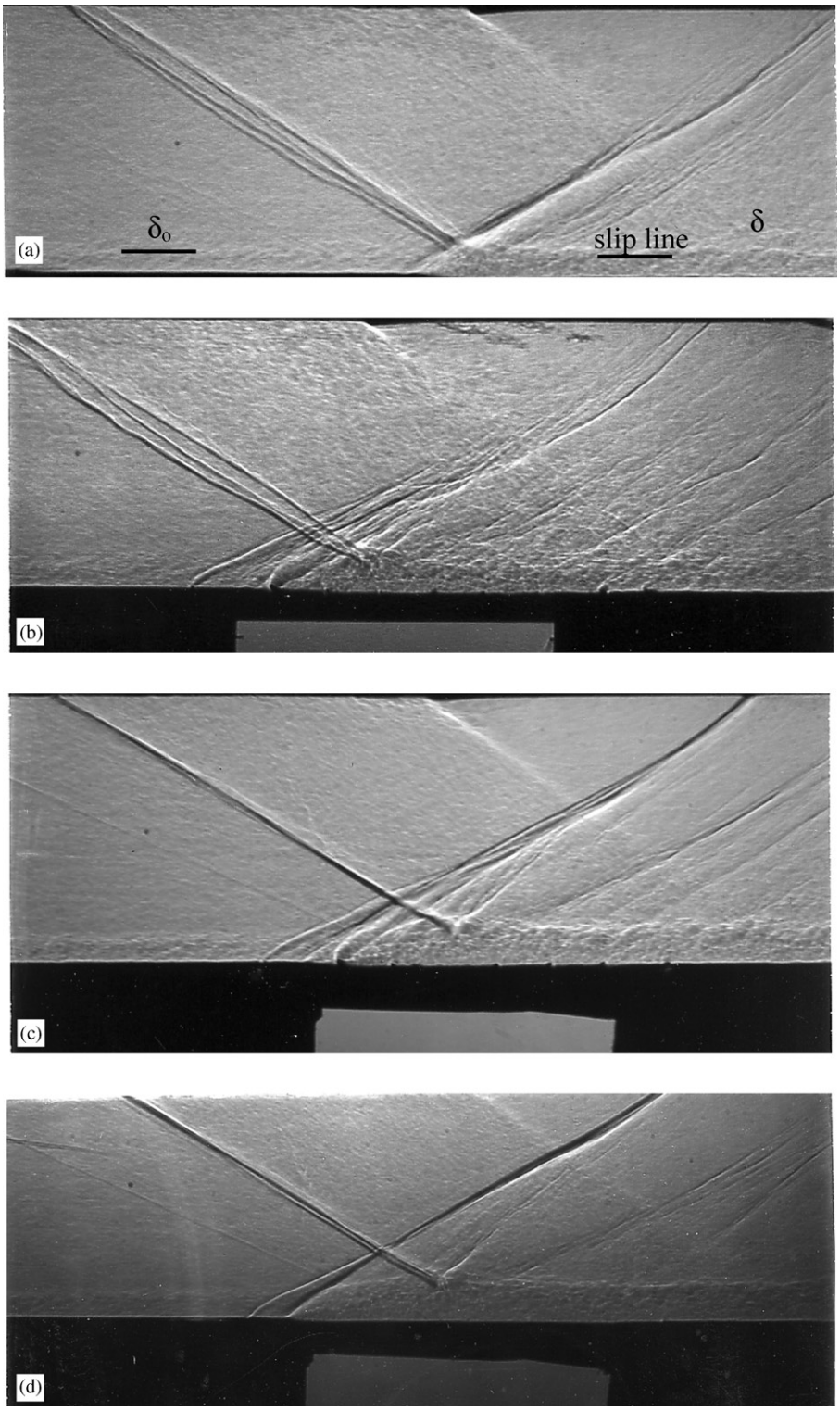

Fig. 5. Shadowgraphs of SBLI: (a) solid-wall case, (b) 127 μm thick second-generation flap array, (c) 127 μm thick, fourth-generation array, and (d) GAC 1897 microporous plate.

result may arise due to the center spar region between the two rows of flaps (see Fig. 3d), which does not allow mass injection or bleed.

A shadowgraph of the GAC 1897 microporous plate, which provides passive transpiration in the SBLI region, is given in Fig. 5d. Close examination reveals several key differences in the flowfield structure as compared to the mesoflap arrays. First, evidence of large rates of transpiration at discrete locations, as seen with the mesoflap arrays, is not detected in this case. This result is a consequence of the smoothly distributed bleed/injection locations, coupled with the low porosity (4%) of the plate, which limits the amount of transpiration. Second, fewer expansion and compression waves are seen downstream of shock impingement due to the continuous nature of the transpiration, and the leading shock appears thinner and more discrete than for the mesoflap experiments. Thirdly, the boundary layer thickness downstream of the interaction did not show improvement over the solid-wall baseline case.

3.3. Wall static pressure measurements

The center-line wall static pressure distribution, normalized by the approach stagnation pressure (581 kPa), is shown in Fig. 6 for the solid wall along with those for various passive control systems. The pressure distribution is nearly constant upstream of shock impingement, and the magnitude is consistent with that for Mach 2.41 approach flow.

As the impending shock impingement is communicated upstream through the subsonic region near the wall, the boundary layer thickens and the pressure slowly increases in response to the weak compression waves that are generated. The pressure rise across the shock for the solid-wall case is diffused over approximately 20 mm ($5.0\delta_0$). The pressure downstream of the interaction is approximately constant until it decreases due to the impingement of the expansion fan produced at the tip of the shock generator. Inflection points can be inferred from these distributions and are marked by the three stars in Fig. 6. The first two indicate the approximate locations of separation ($x^* = -2$) and onset of reattachment ($x^* = 1$), yielding a separation bubble about $3\delta_0$ in length. This rough estimate is corroborated by the LDV results in the SBLI region for the solid wall (to be discussed).

Near the interaction and just downstream, the center-line pressure distribution is changed significantly with the MART system and the microporous plate installed, as highlighted in Fig. 6. The flap thickness in the plot is 127 μm for all mesoflap generations. With either the mesoflap arrays or microporous plate installed, the pressure rise preceding oblique shock impingement is shifted upstream. This offset is due to small differences in the cross-sectional area which occurred when the wind tunnel was taken apart and reassembled between the solid-wall tests and the mesoflap and microporous plate tests. Note that a solid-wall insert case yielded identical upstream pressure values as with the mesoflap cases, but was not deemed suitable as a baseline case as it had small surface perturbations at the insert edges.

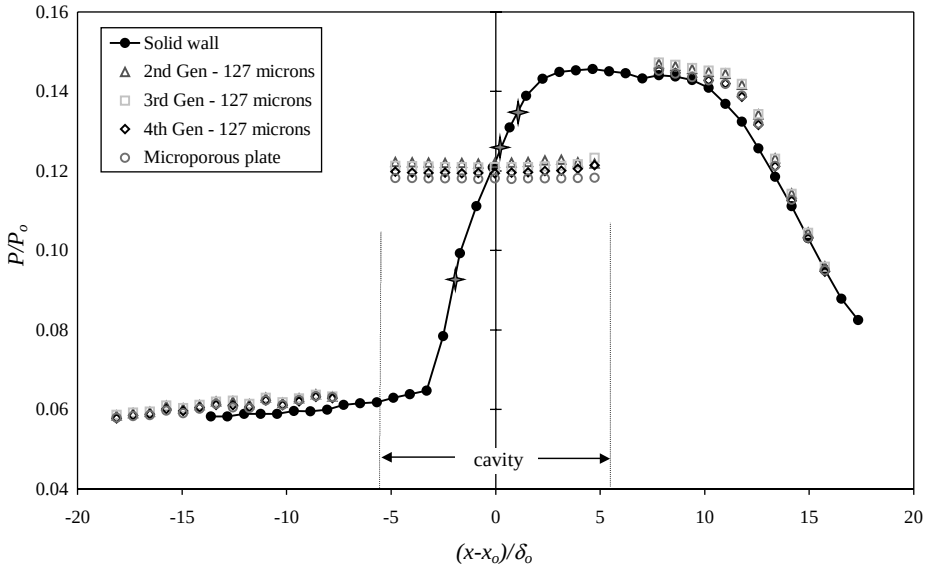

Fig. 6. Center-line surface pressure measurements for SBLI with and without passive control.

Downstream of the cavity, the static pressure ratio for the second- and third-generation mesoflaps is significantly higher than that for the baseline solid-wall case. The fourth-generation flaps and microporous plate produce a static pressure ratio that lies between that for the aforementioned arrays and the solid wall, indicating that these cases did not yield as high of an aerodynamic performance since static pressure recovery was found to be critical to the recirculating transpiration concept (Gefroh, 2000). The pressure at the bottom of the cavity is relatively constant for all cases which is consistent with the behavior for porous plate SBLI control (Bur et al., 1998). The leading oblique shock created by flow injection at the first flap compresses the flow, resulting in a cavity pressure about 12% higher than the average of the pressures before and after shock impingement.

3.4. Velocity measurements

LDV measurements were obtained for the solid-wall baseline study and a variety of thicknesses of all mesoflap generations (no measurements are reported for the microporous plate since the LDV seed blocked many of the microholes). The streamwise velocity characteristics were mapped with 20 streamwise-spaced boundary-layer profiles on the spanwise mid-plane of the tunnel with approximately 42 transverse measurements at each station. While no spanwise measurements were conducted in this study, similar experiments on a solid-wall case and a mesoflap case with an oblique-shock interaction were conducted at NASA Glenn Research Center (GRC). The GRC experiments employed a Mach 2 wind tunnel with a 12:1 ratio of channel width to incoming boundary-layer thickness (the ratio was 19:1 for the present studies) and obtained surface flow visualizations (Loth, 2000). In general, the flow separation regions in the GRC experiments for both the solid-wall and mesoflap cases were found to be approximately two-dimensional near the center-line, but significant sidewall interaction effects appear to be present and significant three-dimensionality was noted near the streamwise edges of the upstream mesoflaps.

Figs. 7–9 are contour plots of the solid-wall and MART array flowfields generated from the streamwise-spaced LDV measurement profiles. In all the following contour plots, the streamwise and transverse coordinates (horizontal and vertical scales) are both normalized by δ_0, and the origin of the horizontal axis is at $x = x_0$. The streamwise mean velocity and r.m.s. velocity fluctuation profiles are both normalized by the incoming freestream velocity ($U_0 = 569$ m/s).

In Fig. 7a, the Mach number contours are shown within the solid-wall SBLI, along with a solid contour line tracing the sonic boundary-layer thickness. From this figure, most of the classic flow features of a solid-wall SBLI can be seen. The boundary layer grows rapidly starting around $x^* = -2$, where a separation bubble also begins to form. The SBLI creates a region of flow reversal between $x^* = -2$ and 1, with a peak height of approximately $0.2\delta_0$. The separation bubble is more clearly seen in corresponding color velocity contour plots (not shown here) where negative velocities can

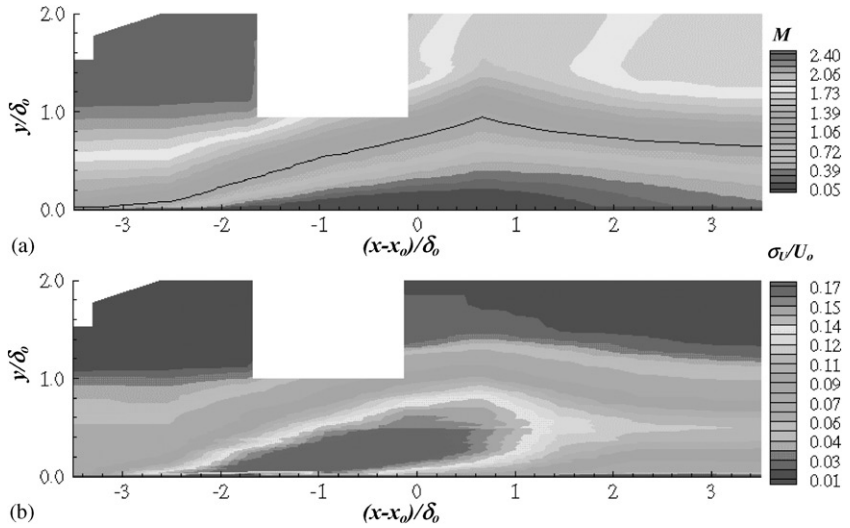

Fig. 7. Solid-wall flowfield surrounding shock impingement where the region between $(x - x_0)/\delta_0 = -2$ and 1 for $y/\delta_0 < 0.2$ is separated flow: (a) Mach number contours with the sonic thickness indicated by the black line and (b) streamwise turbulence intensity (σ_U/U_0) contours. Note, the whited-out region near $x^* = -1$ indicates data could not be properly obtained in this region due to a defect in a test-section window.

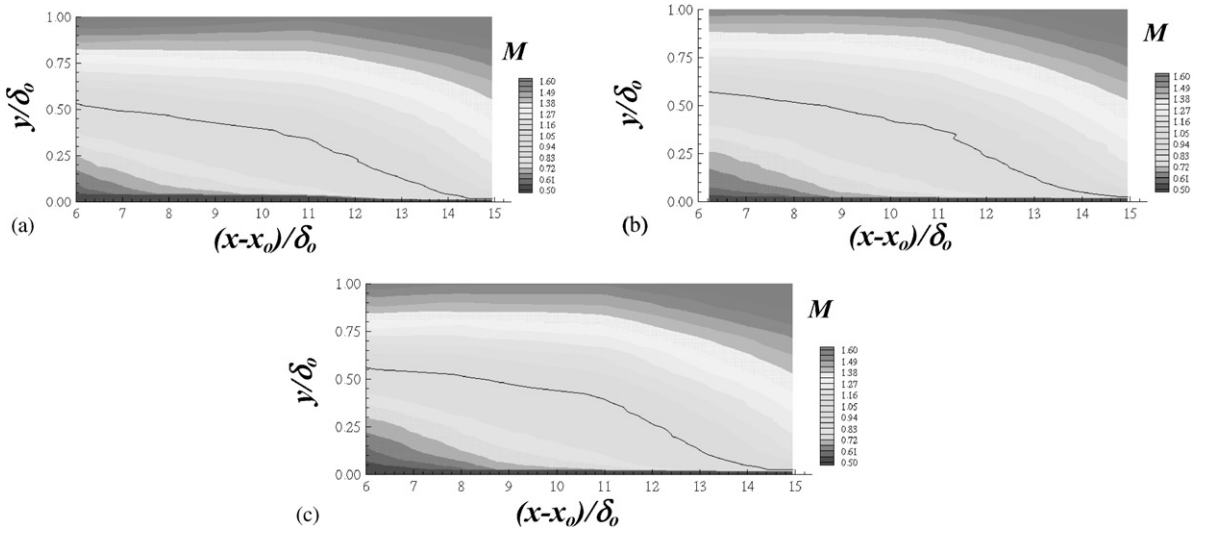

Fig. 8. Outgoing Mach number contours with enhanced y/δ_0 scale (4:1); the sonic boundary layer thickness is indicated by the solid contour line, for: (a) solid-wall case, (b) third-generation aluminum MART array ($t = 127\,\mu m$), and (c) for fourth-generation aluminum MART array ($t = 127\,\mu m$).

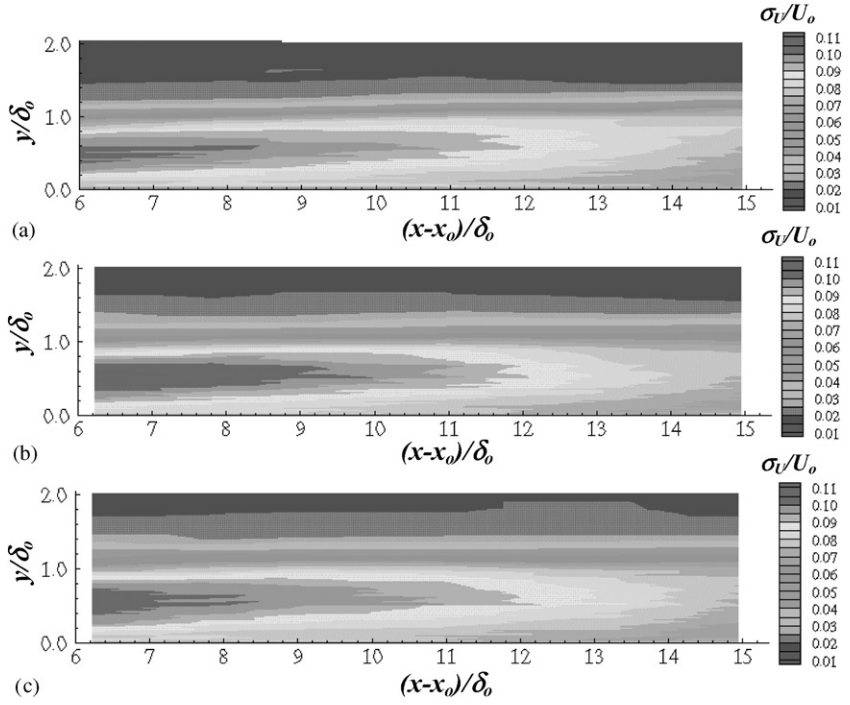

Fig. 9. Outgoing streamwise turbulence intensity (σ_U/U_0) contours for: (a) solid-wall, (b) third-generation aluminum MART array, $t = 127\,\mu m$, and (c) fourth-generation aluminum MART array, $t = 127\,\mu m$.

be noted (Gefroh, 2000). Fig. 7a shows that the sonic line height increases by a factor of 16 over this region, peaking near $x^* = 0.7$ at a value of $0.94\delta_0$. The sonic line height then decreases, reaching a value of $0.64\delta_0$ at $x^* = 3.5$.

Fig. 7b shows the streamwise turbulence intensity (σ_U/U_0) generated within the solid-wall SBLI, where there is high intensity surrounding shock impingement, from $x^* = -2.5$ to 1. The area of high turbulence detaches from the wall

near $x^* = 0$ and rises just as the boundary layer thickness increases. The slip-line shear layer pointed out in the shadowgraphs can be seen to extend downstream near the transverse center of the boundary layer; the peak turbulence intensity is reduced with downstream distance. From this figure, it appears that the wall-normal position of peak turbulence at $x^* = 3$ is at $y/\delta_0 = 0.5$.

The outgoing Mach number contours for the solid-wall and two MART control cases are presented in Figs. 8a–c. In these plots, the ordinate scale is enlarged by a factor of 4:1 and is restricted to $y/\delta_0 < 1$ for enhanced resolution of the boundary-layer and sonic line location. The plot scale shows the boundary-layer recovery region from x locations of 6 to $15\delta_0$ downstream of shock impingement. Fig. 8a presents the Mach contours for the solid-wall baseline case. At $6\delta_0$ downstream, the sonic thickness is $0.53\delta_0$ and decreases steadily to a value of $0.01\delta_0$ at $x^* = 15$ downstream of shock impingement. The initial effects of expansion fan impingement can be seen around $x^* = 11$ (consistent with the shadowgraph and the static pressure data) where the freestream velocity begins to increase.

The general trends exhibited in the Mach number contours of the 127 μm thick third-generation array (Fig. 8b) are nearly identical to the contour plot for the baseline study. However, at $12\delta_0$ downstream, the sonic line height is $0.23\delta_0$, an 8% reduction over the solid wall, indicating the success of the SBLI flow-control concept. In the 127 μm thick fourth-generation array Mach contour plot (Fig. 8c), the sonic thickness at $x^* = 12$ is $0.27\delta_0$, which is larger than for both the solid-wall and third-generation flaps. This indicates that the absence of flaps along the spanwise center-line has reduced the local performance of the array.

The solid-wall turbulence intensity contour plot over the downstream region (Fig. 9a) clearly shows the presence of the slip-line shear layer persisting well beyond $14\delta_0$ downstream of shock impingement. The location of maximum turbulence intensity within the shear layer at $x^* = 6$ is at $y/\delta_0 = 0.5$, and the transverse location increases with downstream distance. At $12\delta_0$ downstream of shock impingement, the transverse location of the maximum turbulence intensity is 33% higher than the height at $6\delta_0$ downstream. For the solid-wall reference case, the turbulence intensity contour corresponding to $\sigma_U/U_0 = 9\%$ persists until $x^* = 12$.

The turbulence intensity contours for the third-generation 127-μm thick flaps are given in Fig. 9b, and indicate strong similarities with the solid-wall data. This figure also shows that the internal shear layer persists beyond $15\delta_0$ downstream of shock impingement, indicating that the boundary layer will require a significant distance to recover to equilibrium conditions. In Fig. 9c, the turbulence intensity contours for the fourth-generation MART array of the same thickness exhibit the same trends as for the third-generation array.

Fig. 10 depicts the Mach number profiles for the aluminum mesoflaps at $x^* = 13.4$. At this location, the outer portion of the boundary layer is immersed in the expansion fan, so the freestream velocity (and Mach number) in all cases continues to increase slightly with distance away from the wall. The 127 μm thick second- and third-generation flaps share nearly identical profiles and appear to lie nearly coincident with the solid-wall data, at least close to the wall. The

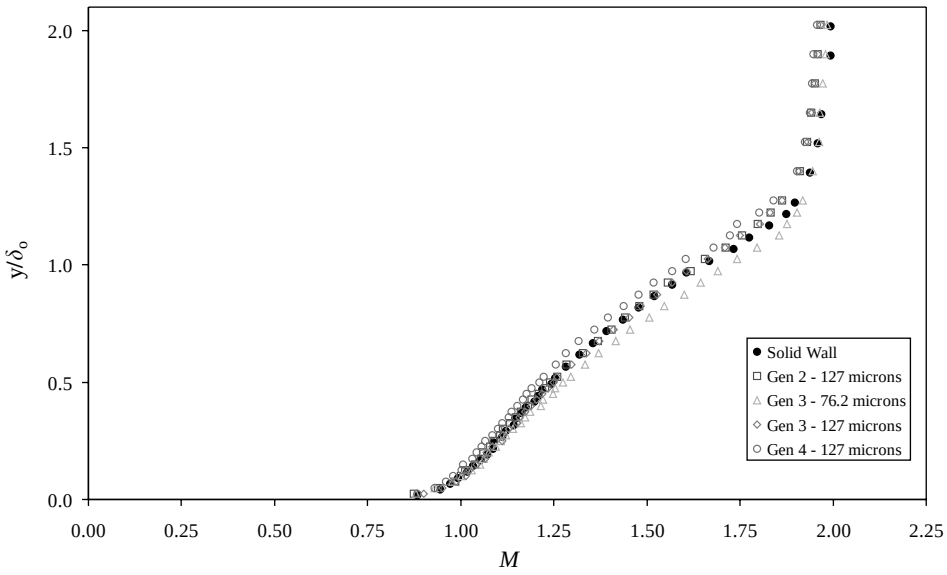

Fig. 10. Outgoing boundary-layer Mach number profiles at $(x - x_0)/\delta_0 = 13.4$ for aluminum mesoflaps.

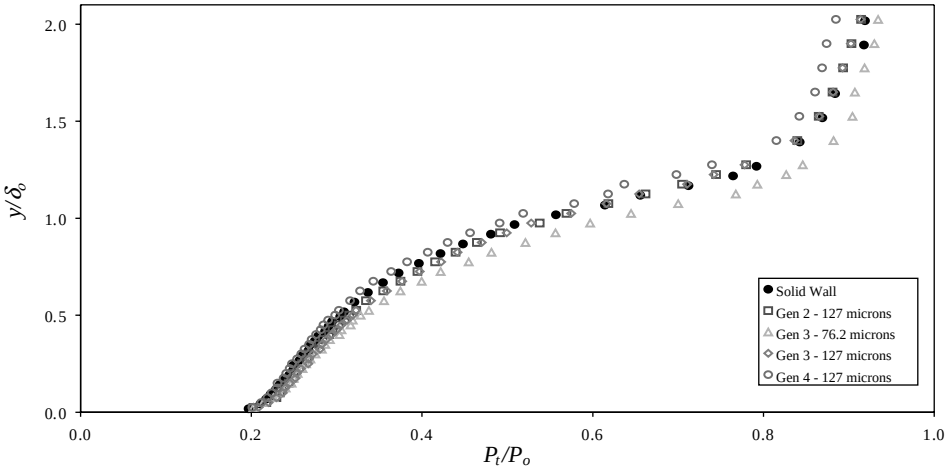

Fig. 11. Outgoing boundary layer stagnation pressure profiles at $(x - x_0)/\delta_0 = 13.4$ for aluminum mesoflaps.

third-generation, 76.2 μm thick flaps provide a much fuller Mach number profile and reduce the boundary-layer thickness by about 7% when compared to the solid-wall baseline. The 76.2 μm thick third-generation mesoflaps deflected considerably, and the resulting boundary layer is improved significantly as compared to the thicker flaps. It is clear, however, that the fourth-generation mesoflap array has the least full Mach number profile and the thickest boundary layer of all cases. Thus, it can be concluded that the three-dimensional effects associated with having a streamwise-running spar along the center-line of the MART array have a deleterious impact on downstream boundary layer characteristics, at least when measuring on the center-line, as done here. However, measurements distributed across the span of the flaps should be obtained to determine whether this observation holds for noncenter-line locations.

An important parameter for the design of supersonic inlets is the magnitude of the stagnation pressure recovery at the engine compressor face after all SBLIs have taken place. The stagnation pressure can be measured using a pitot rake, but for the current test-section this intrusive technique was found to severely alter the boundary layer that was being measured (Gefroh, 2000). Instead, Mach number profiles generated with the LDV measurements (as in Fig. 10) were combined with the wall static pressure at the same station to generate the corresponding stagnation pressure profile from the isentropic relation. This assumes that the transverse static pressure profile is constant, which was confirmed to within 0.5% by numerical simulations of the flow. The resulting stagnation pressure profiles for $x^* = 13.4$ are shown in Fig. 11. In the outer portion of the boundary layer, the stagnation pressure recovery of the second- and third-generation 127 μm thick arrays is nearly identical to that of the solid-wall baseline. The total estimated pressure recovery of the fourth-generation 127 μm array is substantially reduced compared to the solid wall, while that of the 76.2 μm third-generation array is significantly higher (by about 4% of the freestream level) in this region. The latter observation results because the mass injection from the upstream flaps thickens the boundary layer and causes a leading shock to form further upstream than for the baseline case, so that the intersection between the leading and incident shock occurs further from the wall. Therefore, the stagnation pressure recovery with passive control can reap benefits from the "lambda-shock effect" (weakening and diffusion of the compression) over a greater transverse distance than that of the no-bleed case. In addition, the total pressure recovery of the mesoflaps of the current study approximately matches the recovery of the solid-wall baseline close to the wall, suggesting that the angled, passive injection/bleed of the MART system outperforms a conventional perforated plate in terms of the near-wall stagnation pressure recovery. These results suggest that further gains may potentially be obtained with thinner flaps that can withstand the structural demands of large deflections.

4. Conclusions

Experimental investigations were performed to investigate the Mesoflaps for Aeroelastic Recirculating Transpiration (MART) concept for controlling oblique shock/boundary layer interactions (SBLIs) using shadowgraphs, surface pressure, and laser Doppler velocimetry (LDV) measurements. The effect of altering the flap deflections, and thus transpiration characteristics, was investigated by changing the thickness of the flap array and the geometry of the

underlying flap support structure. A variety of different flap designs and thicknesses was studied and compared to the solid-wall, no-bleed baseline case. The results indicate that the flap and spar structural design are critical to ensure flap survivability in this supersonic flow. As compared to aluminum, construction of the surface skin with Nitinol yielded improved structural performance, but yielded approximately the same aerodynamic performance (for the same flap geometries and dimensions). The issue of flap flutter is of special interest, and it may be important to analyze this aspect in more detail (theoretically and/or experimentally).

Shadowgraph photos indicated that the mesoflap deflections and the microporous plate configuration significantly altered the gas dynamic flowfield, especially upstream of the incoming oblique shock where upstream injection yielded ramp-type oblique shock waves. Aerodynamic evidence of improved post-shock boundary layer characteristics along the spanwise center (as compared to the solid-wall case) from the LDV measurements was seen for several, but not all, MART array configurations (note that LDV was not possible for the micro-porous case). The thinnest MART arrays showed evidence of reduced boundary layer thickness downstream of the interaction (by about 7%) as a result of the tangential bleeding of the last flaps. The static pressure measurements indicated that the second- and third-generation mesoflap configurations yielded the highest cavity and downstream static pressure recovery, better than for the microporous plate case, which in turn was better than for the solid-wall case. Estimated stagnation pressure profiles with and without the mesoflaps installed showed better pressure recovery downstream of the SBLI for the mesoflap arrays with the largest deflections (i.e., thinnest flaps). Most likely, this superior pressure recovery with the MART system over the baseline case (and the microporous plate case) is primarily a consequence of the diffused shock footprint caused by upstream mass injection, as detailed in the shadowgraphs. The LDV results also showed quantitative evidence that the MART system can outperform the solid-wall baseline in terms of downstream boundary-layer characteristics. In particular, the thinnest mesoflaps (76.2 μm) showed beneficial effects on the downstream boundary-layer thickness (approximately 7% reduction), whereas some of the thicker flaps did not yield improvements over the solid-wall case. In general, increased performance was attributed to increasing flap deflection (associated with the thinnest flaps) because of the resultingly larger flow recirculation rates for these cases. Improvements in this concept may come from flap array configurations that allow even greater deflections. In addition, hybrid schemes may also be considered for the flow recirculation, e.g., use of the microporous material for the upstream injection portion (to minimize boundary layer intrusion) and flaps for the downstream bleed portion (to minimize flow separation and to maximize removal of low-speed fluid). In addition, further work is needed to systematically investigate the aerodynamic and structural parameters (e.g., flap number, flap shape, flap taper, etc.) in order to establish a robust flow control system.

Acknowledgements

This work was supported under contract F49620-98-1-0490 by the Defense Advanced Research Projects Agency (DARPA) with Dr. Rich Wlezien as technical monitor and the Air Force Office of Scientific Research (AFOSR) with Dr. Steven Walker as technical monitor.

References

Amatucci, V.A., 1990. An experimental investigation of the two-stream, supersonic, near-wake flowfield behind a finite-thickness base. Ph.D. Thesis, Department of Mechanical and Industrial Engineering, University of Illinois at Urbana-Champaign, Urbana, IL, USA.

Bloomberg, J.E., 1989. An investigation of particle dynamics effects related to ldv measurements in compressible flows. M.S. Thesis, Department of Mechanical and Industrial Engineering, University of Illinois at Urbana-Champaign, Urbana, IL, USA.

Bur, R., Corbel, B., Delery, J., 1998. Study of passive control in a transonic shock-wave/boundary layer interaction. AIAA Journal 36, 394–400.

Carroll, B.F., Dutton, J.C., 1992. Turbulence phenomena in a multiple normal shock wave/turbulent boundary layer interaction. AIAA Journal 30, 441–448.

Gefroh, D.L., 2000. Experimental study of mesoflaps to control oblique-shock/boundary-layer interaction. M.S. Thesis, Department of Aeronautical and Astronautical Engineering, University of Illinois at Urbana-Champaign, Urbana, IL, USA.

Gefroh, D.L., Hafenrichter, E.S., Ford, B.M., Dutton, J.C., McIlwain, S.T., Loth, E., 2000a. Experimental study of mesoflaps for SBLI control. 38th AIAA Aerospace Sciences Meeting, AIAA 2000-0355, Reno, NV, USA.

Gefroh, D.L., Hafenricheter, E.S., Dutton, J.C., McIlwain, S., Loth, E., Geubelle, P.G., 2000b. Simulation and experimental analysis of a novel SBLI flow control system. AIAA Fluid Dynamics 2000, AIAA 2000-2237, Denver, CO.

Gridley, M.C., Walker, S.H., 1996. Advanced aero-engine concepts and controls, AGARD Conference Proceeding 572, 86th Symposium, Seattle, WA, USA.

Hamed, A., Yeuan, J.J., Shih, S.H., 1995. Shock-wave/boundary-layer interactions with bleed. Part 1: effect of slot angle. Journal of Propulsion and Power 11, 1231–1235.

Harloff, G.J., Smith, G.E., 1996. Supersonic-inlet boundary layer bleed flow. AIAA Journal 34, 778–785.

Herrin, J.L., Dutton, J.C., 1993. An investigation of LDV velocity bias correction techniques for high-speed separated flows. Experiments in Fluids 14, 354–363.

Hwang, D.P., 2000. An experimental study of turbulent skin friction reduction in supersonic flow using a microblowing technique. 38th AIAA Aerospace Sciences Meeting, AIAA 2000-0545, Reno, NV, USA.

Laurendeau, E., 1995. Boundary-layer bleed roughness. Ph.D. Dissertation, Department of Aeronautics and Astronautics, University of Washington, Seattle, WA, USA.

Loth, E., 2000. Smart mesoflaps for control of shock boundary-layer interactions. AIAA Fluid Dynamics 2000, AIAA-2000-2476, Denver, CO, USA.

Palko, C.W., Dutton, J.C., 1999. A method for separating shock wave motion and turbulence in LDV measurements. Experiments in Fluids 26, 358–370.

Raghunathan, S., 1988. Passive control of shock boundary layer interaction. Progress in Aerospace Sciences 5, 271–296.

Raghunathan, S., McIlwain, S.T., 1990. Further investigations of transonic shock-wave boundary-layer interaction with passive control. Journal of Aircraft 27, 60–65.

Squire, L.C., 1998. A review of the role of some small high-speed wind tunnels in aeronautical research. Progress in Aerospace Sciences 34, 107–166.

Stanewsky, E., Delery, J., Fulker, J., Geibler, W., 1997. Euroshock—drag reduction by passive shock control. Notes on Numerical Fluid Mechanics, 56.

Syberg, J., Hickcox, T.E., 1973. Design of a bleed system for a mach 3.5 inlet. NASA CR-2187.

Wood, B., Loth, E., Geubelle, P., 1999. Mesoflaps for aeroelastic recirculating transpiration for SBLI control. 37th AIAA Aerospace Sciences Meeting, AIAA 99-0614, Reno, NV, USA.